

Biswajit Bhattacharyya | Christian Balischewski | Eric Sperlich |  
Christina Günter | Stefan Mies | Alexandra Kelling | Andreas Taubert

## N-Butyl Pyridinium Diiodido Argentate(I)

A One-Dimensional Ag-I Network with Superior Solid-State Ionic  
Conductivity at Room Temperature

**Suggested citation referring to the original publication:**

Advanced materials interfaces 10 (2023) 12  
DOI <https://doi.org/10.1002/admi.202202363>  
ISSN 2196-7350

**Journal article | Version of record**

Secondary publication archived on the Publication Server of the University of Potsdam:  
Zweitveröffentlichungen der Universität Potsdam : Mathematisch-Naturwissenschaft-  
liche Reihe 1341  
ISSN: 2196-7350  
<https://nbn-resolving.org/urn:nbn:de:kobv:517-opus4-604874>  
DOI: <https://doi.org/10.25932/publishup-60487>

**Terms of use:**

This work is licensed under a Creative Commons License. This does not apply to quoted  
content from other authors. To view a copy of this license visit  
<https://creativecommons.org/licenses/by/4.0/>.

# N-Butyl Pyridinium Diiodido Argentate(I): A One-Dimensional Ag-I Network with Superior Solid-State Ionic Conductivity at Room Temperature

Biswajit Bhattacharyya,\* Christian Balischewski, Eric Sperlich, Christina Günter, Stefan Mies, Alexandra Kelling, and Andreas Taubert\*

A new solid-state material, N-butyl pyridinium diiodido argentate(I), is synthesized using a simple and effective one-pot approach. In the solid state, the compound exhibits 1D  $[\text{AgI}_2]^-$  chains that are stabilized by the N-butyl pyridinium cation. The 1D structure is further manifested by the formation of long, needle-like crystals, as revealed from electron microscopy. As the general composition is derived from metal halide-based ionic liquids, the compound has a low melting point of 100–101 °C, as confirmed by differential scanning calorimetry. Most importantly, the compound has a conductivity of  $10^{-6} \text{ S cm}^{-1}$  at room temperature. At higher temperatures the conductivity increases and reaches to  $10^{-4} \text{ S cm}^{-1}$  at 70 °C. In contrast to AgI, however, the current material has a highly anisotropic 1D arrangement of the ionic domains. This provides direct and tuneable access to fast and anisotropic ionic conduction. The material is thus a significant step forward beyond current ion conductors and a highly promising prototype for the rational design of highly conductive ionic solid-state conductors for battery or solar cell applications.

gas sensors,<sup>[9,10]</sup> battery electrolytes,<sup>[11–13]</sup> for catalysis<sup>[14,15]</sup> etc. A further advantage is that many solid ionic conductors can easily be patterned or shaped in device fabrication processes to match certain requirements.<sup>[5,13,16]</sup> Among all solid ionic conductors, silver halide based ionic conductors are arguably the most intensely researched compounds.<sup>[17,18]</sup> Among these,  $\alpha$ -AgI is of particular interest because it shows superionic ionic conductivity as high as  $1 \text{ S cm}^{-1}$ <sup>[19–21]</sup> However,  $\alpha$ -AgI only forms above 147 °C.<sup>[22,23]</sup> The room temperature phases of this material are  $\beta$ -AgI and polycrystalline AgI. Both have a low ionic conductivity on the order of  $10^{-6} \text{ S cm}^{-1}$ ,<sup>[24,25]</sup> which also does not change significantly with temperature. As a result, there is a clear need for low cost-high performance ionic conductors with a structure that can be modulated at will to

adjust their properties.<sup>[26,27]</sup>


Here we report the first prototype of such a modular material, N-butyl pyridinium diiodido argentate(I),  $(\text{C}_4\text{Py})[\text{AgI}_2]$ . The synthesis is straightforward, the material is obtained as a pure crystalline product, and the most prominent feature is a highly anisotropic crystals structure, where the basic building block  $[\text{AgI}_2]^-$  forms infinite chains in 1D around a central  $\text{Ag}^+$  ion with four-fold iodide coordination in a rather distorted geometry. As a result, the material shows an ionic conductivity that is almost double than what is observed for AgI at room temperature and one order of magnitude higher than that of AgI when compared at 70 °C. Due to its ease of synthesis and processability, N-butyl pyridinium diiodido argentate(I) is a highly interesting candidate for solid state ionic conduction. Its performance is much better than either bulk or nanoscale AgI and it has the added benefit that the material can also easily be modified by adding other ions, similar ionic materials based on the  $[\text{MX}_4]^{2-}$  cations, where addition or change of a 3d metal or a halide ligand changes optical properties and ionic conduction.<sup>[28,29]</sup>

## 1. Introduction

Organic–inorganic metal halides are important materials for the next generation optoelectronic applications.<sup>[1–3]</sup> Whether the phase is perovskite or non-perovskite, these materials have been extensively used as light emitting solid state materials,<sup>[4–8]</sup>

B. Bhattacharyya, C. Balischewski, E. Sperlich, S. Mies, A. Kelling, A. Taubert  
 Institute of Chemistry  
 University of Potsdam  
 14476 Potsdam, Germany  
 E-mail: bhattacharyya@uni-potsdam.de; ataubert@uni-potsdam.de

C. Günter  
 Institute of Geosciences  
 University of Potsdam  
 14476 Potsdam, Germany

 The ORCID identification number(s) for the author(s) of this article can be found under <https://doi.org/10.1002/admi.202202363>.

© 2023 The Authors. Advanced Materials Interfaces published by Wiley-VCH GmbH. This is an open access article under the terms of the Creative Commons Attribution License, which permits use, distribution and reproduction in any medium, provided the original work is properly cited.

DOI: 10.1002/admi.202202363

## 2. Results and Discussion

$(\text{C}_4\text{Py})[\text{AgI}_2]$  can be synthesized in a single step method in very good yields, see Experimental Section for details. In short, the

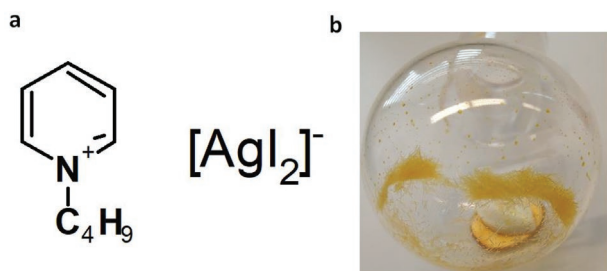


**Figure 1.** a) Principal structural unit of *N*-butyl pyridinium diiodoargentate(I). b) Photograph of some crystals obtained directly after cooling the reaction mixture.

precursors are mixed in acetonitrile, heated to reflux, and then allowed to cool to room temperature. After a few hours, the crystalline product directly precipitates as yellow crystals that can directly be analyzed with single crystal X-ray diffraction. **Figure 1a,b** shows the basic building blocks, the reaction scheme, and a representative photograph of some of the precipitated product.

**Figure 2a** shows SEM images of the needle shaped crystalline compound. All crystals exhibit smooth faces and rather clear edges indicating a high quality. Additional energy dispersive X-ray (EDX) analysis of these structures (**Figure S1**, Supporting Information) reveals that the silver content amounts to 33% and iodine is 67%. This is consistent with the stoichiometry shown in **Figure 1**, suggesting that the basic building block is indeed the  $[\text{AgI}_2]^-$  unit.

**Figure 2b** shows a representative IR spectrum of the crystalline material. Similar to other halidometallate compounds, the spectra of the current material mostly show bands that can be assigned to the organic cation, *N*-butyl pyridinium. Bands at  $1630$  and  $1490\text{ cm}^{-1}$  are from C=C and C=N stretching vibrations of the pyridinium ring. Bands at  $175$  and  $985\text{ cm}^{-1}$  are from the exocyclic C–N stretching of the substituted alkylated chain.<sup>[28,29]</sup> Overall the IR spectra confirm that the organic cation is present in the compound.

A further understanding of the structure and structure-property relations can be derived from the single crystal structure (**Figures 3** and **4**). The compound  $(\text{C}_4\text{Py})[\text{AgI}_2]$  crystallizes in the monoclinic space group  $P2_1$  with four formula units per

unit cell. **Table S1** (Supporting Information) shows the crystallographic data and structural refinement of the compound. There are two *N*-butyl-pyridinium cations and one  $[\text{Ag}_2\text{I}_4]^{2-}$  anion fragment in the asymmetric unit, matching with the EDX analysis presented in **Figure S1** (Supporting Information). **Figure 3** shows the atoms in ellipsoid view with atom labeling. In one of the cations there is a disorder of the C17 and C18 atoms of the butyl chain with an occupation of part A (labeled in red in **Figure 3**) with 66% and part B (labeled in green) with 34%. Within the anion, every Ag cation is tetrahedrally connected to four iodide anions, the iodide anions are  $\mu^2$  linked between two Ag cations. This results in one-dimensional  $[\text{AgI}_2]^-$  anion chains in the solid-state along the crystallographic *a* axis.

Parallel-displaced stacking interactions are also visible between the cations. This results in an alternating arrangement of the two symmetry-independent cations, along the crystallographic *a*-axis (see **Figure 4a**). Numerous very weak C–H $\cdots$ I hydrogen bonds form between the cations and the anions (**Figure 4b**, left). All anion chains are embedded by a total of three cation stacks each (**Figure 4b**, right). As a result, the anion chains form a 1D anisotropic structure. Structurally these types of arrangements are very important for ionic solids because they could enable highly anisotropic ionic conduction.

**Figure 5** shows additional data obtained from powder X-ray diffraction (PXRD). The experimental and simulated PXRD data of  $(\text{C}_4\text{Py})[\text{AgI}_2]$  exactly match. This demonstrates that (1) the single crystal structure is identical to the structure of the powders isolated directly from the synthesis and (2) that there are no crystalline impurities in the materials.

Besides its structural anisotropy,  $(\text{C}_4\text{Py})[\text{AgI}_2]$  has interesting thermal properties. **Figure 6a** shows differential scanning calorimetry (DSC) data of the compound. First, the compound exhibits a glass transition ( $T_g$ ) at around  $0\text{ }^\circ\text{C}$ . The sharp peak at  $48\text{ }^\circ\text{C}$  indicates a cold crystallization ( $T_c$ ) and the intense signal at  $100.6\text{ }^\circ\text{C}$  stems from a melting transition ( $T_m$ ). Interestingly the compound has a higher melting point than the parent *N*-butyl pyridinium iodide, which has a melting point of  $74\text{ }^\circ\text{C}$ . This melting point increase is probably because of stronger interactions in the  $(\text{C}_4\text{Py})[\text{AgI}_2]$  anionic 1D chains along with further non-covalent interactions. The crystal structure supports this by showing the formation of strong hydrogen bonds and the additional parallel-displaced cation  $\pi$ -stacking interactions. The

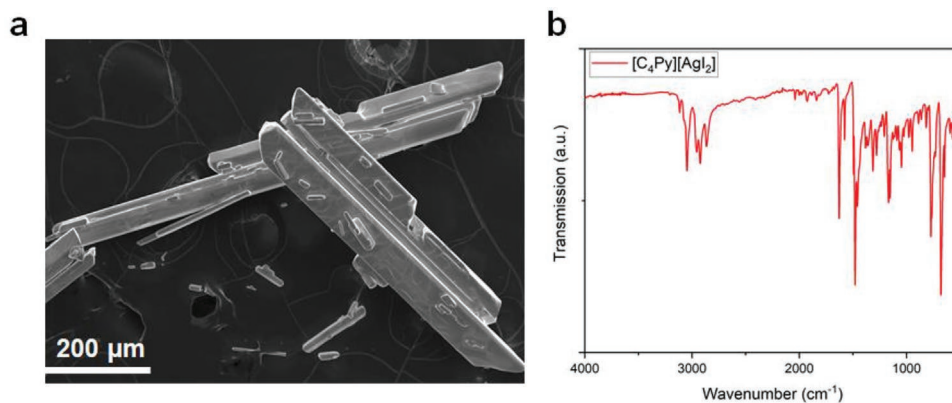


**Figure 2.** a) SEM images of some *N*-butyl pyridinium diiodoargentate(I) microcrystals. b) Attenuated total reflectance IR (ATR-IR) spectrum of the material.

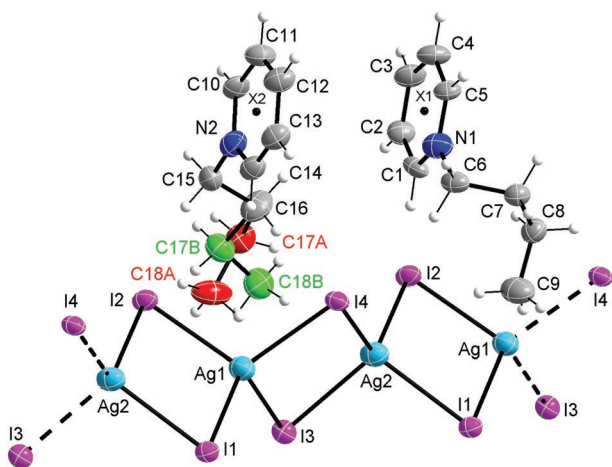


**Figure 3.** Crystal structure of  $[\text{C}_4\text{Py}][\text{AgI}_2]$  with atomic labels. Displacement ellipsoids are shown at the 50% probability level. The disorder in the molecular structure is shown in red (part A) and green (part B). X marks the center of the pyridinium rings.

stronger interactions may lead to a higher melting temperature, as more energy is needed for the transition from solid to liquid state.

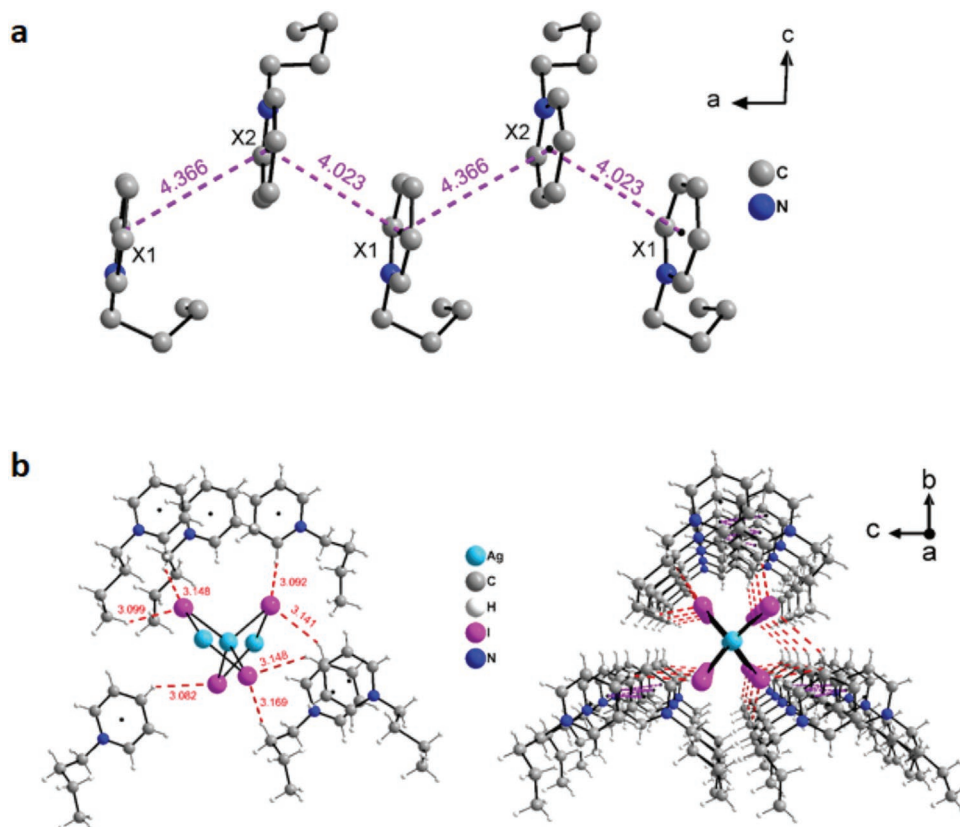
Thermogravimetric analysis (TGA) experiments were performed to assess the material stability. Figure 6b shows that the compound starts decomposing at 250 °C and almost 55% of the compound decomposes up to 350 °C, which can predomi-

nantly be assigned to the elimination of the *N*-butyl pyridinium unit. Between 400 and 850 °C decomposition of  $[\text{AgI}_2]^-$  unit occurs. Ultimately it converts to silver oxide. Further analysis of the TGA data using the first derivative (Figure S3, Supporting Information) shows that there is no minor weight loss from 25 to 100 °C. This implies that the compound is water- and solvent-free, and not hygroscopic, consistent with the single crystal structure described above.

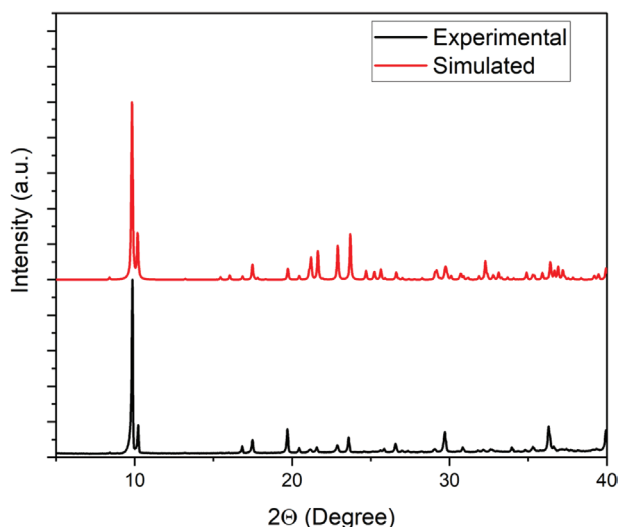
Figure 7 shows the corresponding absorption spectra of  $(\text{C}_4\text{Py})[\text{AgI}_2]$ . The band gap was determined via Tauc plot using the Kubelka–Munk equation, see Experimental Section for details. The estimated band gap is 3.40 eV, Figure 7 (inset). It is therefore larger than the band gap of bulk AgI (2.75 eV).<sup>[30,31]</sup> Interestingly, the absorption band at 3.40 eV is also visible in solution phase absorption spectra of  $(\text{C}_4\text{Py})[\text{AgI}_2]$  (Figure S4, Supporting Information). This may imply that the absorption is due to band to band transition and an exciton-like feature.<sup>[32,33]</sup> The bands at 4.26 and 4.81 eV in the figure are pyridine ring absorption bands.<sup>[34,35]</sup>

Figure 8a shows the temperature-dependent conductivity of  $(\text{C}_4\text{Py})[\text{AgI}_2]$  obtained from impedance analysis (the Nyquist plot with its corresponding electric circuit is displayed in Figure S5, Supporting Information). At 30 °C, the conductivity of the compound is  $1.1 \times 10^{-6} \text{ S cm}^{-1}$ . It increases with temperature and reaches  $1.5 \times 10^{-4} \text{ S cm}^{-1}$  at 70 °C. This is significantly higher than the conductivity of pure AgI bulk crystals.

It is quite important to understand the ionic conduction contribution in the compounds during conductivity measurements. In the ionic conduction measurements, the conductivity,



**Figure 4.** a) Parallel-displaced stacking interactions (purple dotted lines) between the cations (hydrogen atoms are omitted). b) C–H...I hydrogen bonding (red dashed lines) between the cations and anions in  $(\text{C}_4\text{Py})[\text{AgI}_2]$ .



**Figure 5.** Experimental PXRD pattern determined from the crystalline powder and calculated PXRD of the same material; calculation was done from the single crystal structure data shown above.

temperature, and the activation energy can be expressed using the Arrhenius equation,

$$\sigma = (\sigma_0/T) \exp\left(-\frac{E_a}{k_B T}\right) \quad (1)$$

where  $\sigma$  is the ionic conductivity,  $E_a$  is the activation energy,  $k_B$  the Boltzmann constant, and  $\sigma_0$  is a prefactor.

From Equation (1) we obtain,

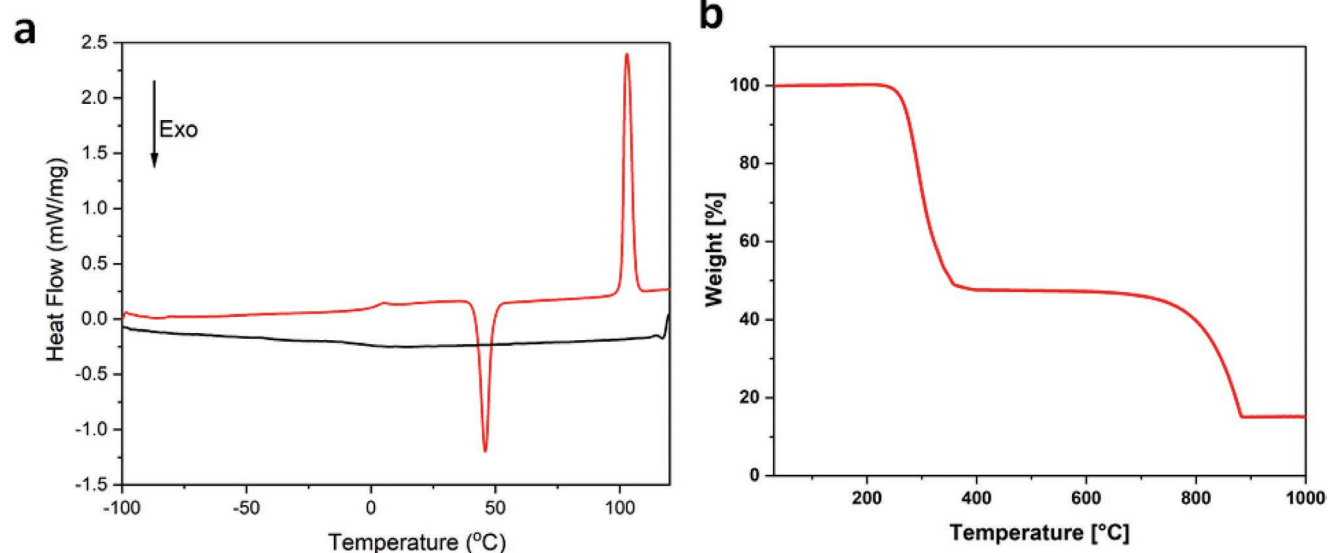
$$E_a = -k_B \left[ \partial \ln(\sigma T) / \partial \left(\frac{1}{T}\right) \right] \quad (2)$$

Figure 8b shows the plot of  $\ln(\sigma T)$  versus  $1000/T$ . Using Equation (2), the activation energy for ionic conduction is calculated, which is 0.278 eV. The Arrhenius plot has a perfect

linear temperature dependence. We have also analyzed the corresponding polarization data to understand the nature of conductivity of these samples. The DC polarization data suggests that the electric contribution in conductivity is negligible in these compounds (Figure S6, Supporting Information). So overall conductivity is ionic in nature. Figure 8c compares the ionic conductivities of  $(C_4Py)[AgI_2]$  with other AgI-based conductors.  $(C_4Py)[AgI_2]$  has a conductivity that is about twice that of polycrystalline AgI at 30 °C. At 70 °C, it is almost one order of magnitude higher than the conductivity observed for the  $\beta$ -phase of bulk AgI, but also two orders of magnitude lower than the conductivity of  $\alpha$ -AgI nanoparticles dispersed in a poly(vinylpyrrolidone) matrix.

Overall, ionic solids such as  $(C_4Py)[AgI_2]$  are interesting materials for a variety of applications and the current example is a highlight in terms of simplicity of synthesis. The current materials are highly promising candidates for solid-state ion conduction and a highly versatile and adaptable prototype for future generations of ion conductors. Considering the low temperature conductivity at 30 °C, it is the best ionic AgI-based solid state conductor currently known at room temperature. At 70 °C, AgI still shows better overall conductivities, but the current system is far superior in terms of adjustability and a “materials by design” approach than any bulk or nanoscale AgI or related compound.

As a result, the approach presented here is clearly challenging plain AgI based-conductors for a multitude of reasons: (1) the current approach is a platform approach allowing for the smart and rational design of ionic solid state conductors by combination of Ag (and other metals) with various ligands (halides, pseudo halides, etc.) to adjust the crystal structure and dynamics to adjust ion mobility, (2) the choice of counter-cation (*N*-butyl pyridinium in the current study) will enable access to 2D or even 1D architectures that will allow for directional ion conduction, and (3) the synthesis is highly flexible and can be completely automated to allow for low-cost-high-throughput



**Figure 6.** a) Representative DSC data of the sample (second heating cycle). Red is heating and black is the cooling curve. b) TGA data of the sample (red line).

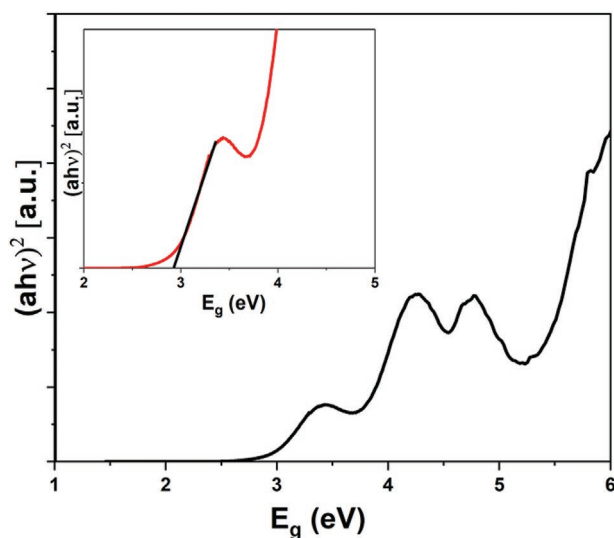


**Figure 7.** Optical absorption of  $(C_4Py)[AgI_2]$  calculated from the UV reflectance data (black line). Inset: Tauc plot for determination of the band gap (red line).

synthesis approaches, e.g., via robotic or flow methods while still being flexible to allow materials tuning on the fly.

### 3. Conclusions

In conclusion, we have reported  $(C_4Py)[AgI_2]$  a transparent low melting organic–inorganic metal halide ionic solid for superior ionic conduction. Along with its simple one pot synthesis, the compound has an interesting 1D anisotropic crystal structure, which appears to be highly favorable for fast ionic conduction.  $(C_4Py)[AgI_2]$  is currently the best Ag-based ion conductor at room temperature and a highly promising prototype for more advanced ion conductors, especially because its composition (and therefore properties) can very easily be adjusted for a specific requirement.

### 4. Experimental Section

**Chemicals:** *N*-butyl pyridinium iodide (iolitec,  $\geq 98.0\%$ ), Silver iodide (VWR,  $\geq 98.0\%$ ), propan-2-ol (VWR  $\geq 99\%$ ), magnesium sulfate AnalaR NORMAPUR (VWR  $\geq 98.0\%$ , CAS 7587–889), acetonitrile (VWR  $\geq 99.9\%$ ), and ferrocene (Alfa Aesar,  $\geq 99\%$ ) were used as received.

**Synthesis:**  $(C_4Py)[AgI_2]$  has been synthesized in a single step method with slight modifications.<sup>[36]</sup> 1000 mg (3.8 mmol) *N*-butyl pyridinium iodide ( $C_4PyI$ ) and an equimolar amount of the silver iodide salt with the ratio of 1:1 (893 mg of AgI) were dissolved in 10 mL acetonitrile. The reaction was held at 110 °C for 90 min under reflux conditions. Then the reaction mixture was cooled and kept at room temperature overnight to allow for the direct precipitation of the crystalline product. These as prepared crystals were sufficient for the further analysis without any additional purification methods. Average yields of the reaction were 85%. The synthesis was repeated up to three times in a single batch for reproducibility.

**Infrared Spectroscopy:** A NICOLET iS5 by THERMO SCIENTIFIC was used for the IR measurements alongside an ID7 ATR-attachment with

a diamond crystal. The samples were measured using ATR mode between 4000 and 400  $cm^{-1}$  with a resolution of 4  $cm^{-1}$ . The sample was measured as a powder.

**Thermogravimetric Analysis:** Thermogravimetric analysis (TGA) was carried out by a Mettler Toledo TGA 2 Thermogravimetric Analyzer (temperature range: 25 to 1000 °C, mass resolution: 0.1 mg) at a heating rate of 10 K  $min^{-1}$  under nitrogen flow in aluminum crucibles.

**Single Crystal Structure Analysis:** A suitable single crystal of the compound was selected using a Leica M205C light microscope and was separated with oil. The X-ray diffraction experiment was carried out on a Stoe Stadivari with monochromated Mo- $K\alpha$  radiation ( $\lambda = 0.71073 \text{ \AA}$ ) and a Pilatus 200 K detector. The measurement was done at 210 K using an Oxford Cryostream cooling device. The data were corrected using the program X-Area<sup>[37]</sup> and the structure was solved by direct methods and refined against  $F^2$  on all data by full-matrix least-squares using the SHELX suite of programs.<sup>[38,39]</sup> The crystal structure was visualized with Diamond.<sup>[40]</sup> The crystallographic data (CCDC-2178254) can be obtained free of charge from the Cambridge Crystallographic Data Centre, <http://www.ccdc.cam.ac.uk>.

**Powder X-Ray Diffraction:** X-ray Powder diffraction data were collected on a PANalytical Empyrean powder X-ray diffractometer in a Bragg–Brentano geometry using Cu  $K\alpha$  radiation ( $\lambda = 1.5419 \text{ \AA}$ ). It was equipped with a programmable divergence and anti-scatter slit and a large Ni-beta filter. The PIXcel1D detector was set to continuous mode with an active length of 3.0061°. Scans were run in a  $2\theta$  range of 4–70° with step size of 0.0131° operating at 40 kV and 40 mA. A sample rotation time of 1 s was used.

**Scanning Electron Microscopy (SEM) Analysis:** Scanning electron microscopy (SEM) was done on a JEOL JSM-6510 SEM (Freising, Germany) with a tungsten cathode operated at 15 kV. Prior to imaging, all samples were sputter-coated with carbon for 75 s and 18 mA using a SC7620 mini sputter-coater (Quorum Technologies, Lewes, UK).

**Differential Scanning Calorimetry:** DSC measurements were done using a Netzsch DSC 214 Polyma at 5–10 K  $min^{-1}$  under nitrogen. Each run consisted of three heating-cooling cycles.

**UV/Vis-Spectroscopy:** UV/vis measurements were conducted using a Lambda 950 by PERKIN ELMER with the solid material attachment Praying Mantis by HARRICK SCIENTIFIC PRODUCTS INC. During the experiments  $MgSO_4$  AnalaR NORMAPUR by VWR was used as a background material. The measuring range was  $\lambda = 850\text{--}250 \text{ nm}$  with a resolution of 2 nm. The Kubelka–Munk Equation (3) was used for the analysis of the UV/vis data.

$$\frac{K}{S} = \frac{(1-R)^2}{2R} \quad (3)$$

$K$  is absorption coefficient,  $S$  is the scattering coefficient, and  $R$  is the reflectance.

Based on the UV/vis analysis the optical band gaps were graphically analyzed using the Tauc plot (3). The plots were then fitted via Origin.

$$(\alpha h\nu)^{1/n} = A(h\nu - E_g) \quad (4)$$

$h$  is the Planck's constant,  $\nu$  is the photon's frequency,  $\alpha$  is the absorption coefficient,  $E_g$  is band gap,  $A$  is the proportionality constant, with the following values for  $n$ ,  $n = 1/2$  for direct allowed transitions,  $n = 3/2$  for direct forbidden transitions,  $n = 2$  for indirect allowed transitions,  $n = 3$  for indirect forbidden transitions.

**Electrical Impedance Spectroscopy:** Impedance spectra were measured as follows: An impedance setup of the Autolab PGSTAT204 system (METROHM GmbH & Co. KG) was used to measure from 500 kHz to 100 Hz with an amplitude of 0.1 V. A temperature-controlled microcell HC (rhd instruments) was used for temperature-dependent measurements, with the measurements carried out at temperatures ranging from 25 to 70 °C. A Peltier element with an accuracy of 0.01 °C conducted heating and cooling. The compounds were prepared as follows: The compound was placed in a separate silicon form and heated to 110 °C in a heating oven, with the temperature then being held for 60 min. Besides removing most of the residual water, this process produced a macroscopic pellet

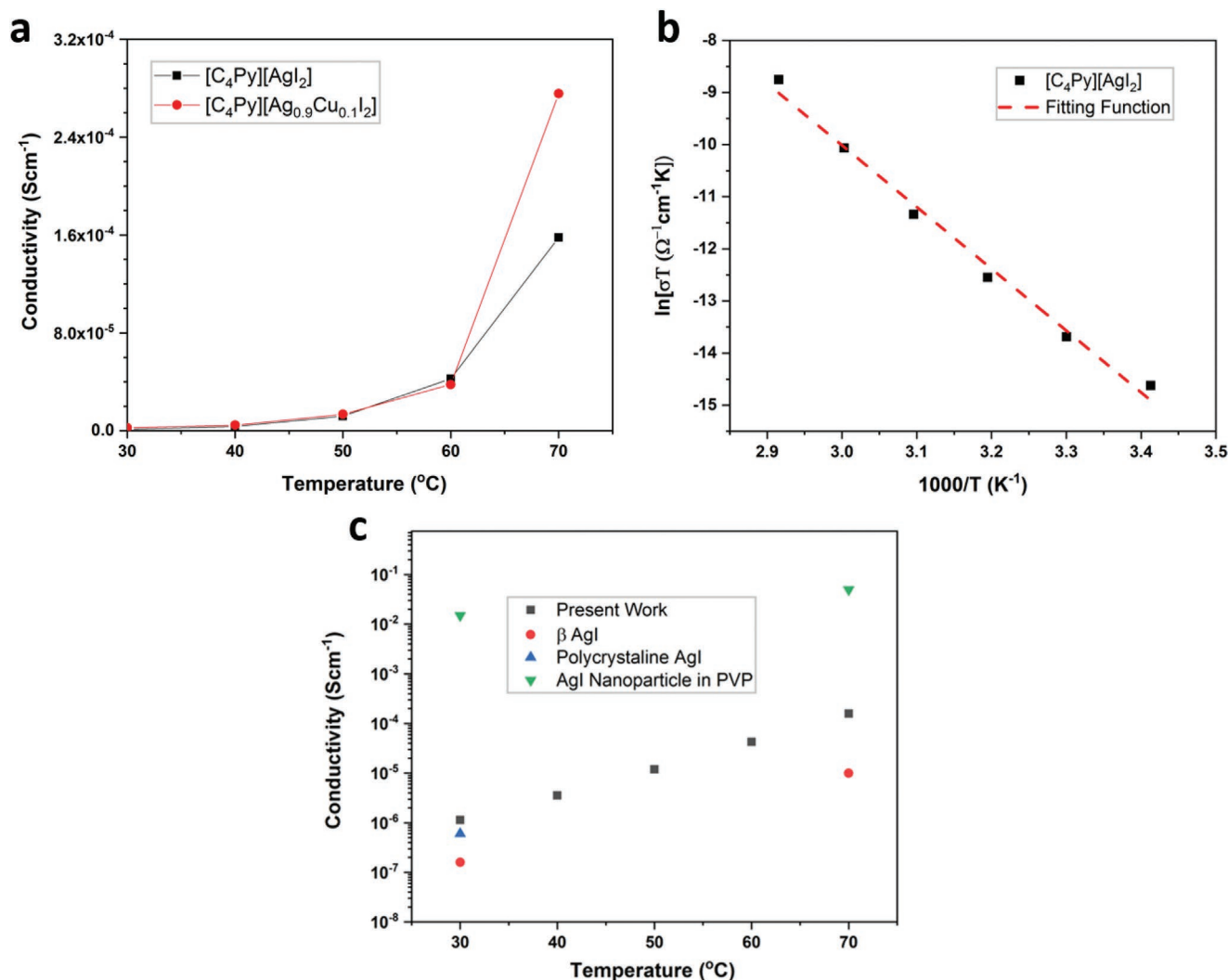


**Figure 8.** a) Conductivity of (C<sub>4</sub>Py)[AgI<sub>2</sub>] (black squares) and (C<sub>4</sub>Py)[Ag<sub>0.9</sub>Cu<sub>0.1</sub>I<sub>2</sub>] (red circles) versus temperature. b) Arrhenius Plot of the (C<sub>4</sub>Py)[AgI<sub>2</sub>] with fitting function to calculate the activation energy for ionic conduction. c) Reference conductivity plot for different AgI conductors. Black squares are data from the current study. Red circles are data from β-AgI bulk structures,<sup>[20,24]</sup> blue triangles are data from polycrystalline AgI,<sup>[25]</sup> and green reverse triangle are data from α-AgI nanoparticles dispersed in poly(vinylpyrrolidone).<sup>[22]</sup>

for usage in the measuring cell. This also ensures a large contact area with the electrodes. The pellet was then placed between the electrodes in the measuring cell. Using Equation (5) the conductivity  $\sigma$  was calculated with  $R$  being the (electrolyte) resistance,  $A$  being the surface content of the circular-shaped electrodes, and  $d$  being the height of the sample, which also is the thickness of the electrode layer.

$$\sigma = \frac{d}{R \cdot A} \quad (5)$$

During the impedance measurements, the performance of the pure ILs was analyzed using a two-electrode cell setup (Pt-electrode, Graphit-electrode) with a rhd TSC battery (Ni-electrodes 9 mm) in combination with a Metrohm Autolab PGSTAT204. To prevent corrosion and degradation of the Ni-electrodes, Au-electrodes were placed between sample and Ni-electrodes. Measurements were done using the NOVA software (Metrohm). Analysis was done using the RelaxIS software (rhd instruments, Marburg, Germany).

## Supporting Information

Supporting Information is available from the Wiley Online Library or from the author.

## Acknowledgements

The authors thank Anne Nitschke for help with TGA and Dr. M. Drüschler (rhd) for help with impedance spectroscopy data analysis. Funding from the University of Potsdam (53170000, A.T.) and the Leistungszentrum Funktionsintegration (B.B.) are gratefully acknowledged.

Open access funding enabled and organized by Projekt DEAL.

## Conflict of Interest

The authors declare no conflict of interest.

## Author Contributions

B.B., A.T. conceived the idea. B.B. synthesized the samples and analyzed the data with help of C.B. The co-authors C.G., E.S., and S.M. helped with the microstructure, single crystal and DSC studies. E.S. performed the single crystal analysis and wrote the corresponding draft

paragraphs. B.B. and A.T. wrote the manuscript. All authors contributed to writing and editing the manuscript.

## Data Availability Statement

The data that support the findings of this study are available from the corresponding author upon reasonable request.

## Keywords

Agl, ionic conductivity, Ionic liquids, thermal properties

Received: November 16, 2022

Revised: February 9, 2023

Published online: March 22, 2023

- [1] J. S. Manser, J. A. Christians, P. V. Kamat, *Chem. Rev.* **2016**, *116*, 12956.
- [2] J. Sun, J. Wu, X. Tong, F. Lin, Y. Wang, Z. M. Wang, *Adv. Sci.* **2018**, *5*, 1700780.
- [3] P.-P. Sun, D. R. Kripalani, M. Hao, W. Chi, W. Li, K. Zhou, *J. Phys. Chem. Lett.* **2020**, *11*, 5234.
- [4] Y.-H. Kim, H. Cho, T.-W. Lee, *PNAS* **2016**, *113*, 11694.
- [5] H. Mo, Y.-C. Yin, J.-D. Luo, J.-T. Yang, F. Li, D.-M. Huang, H. Zhang, B. Ye, T. Tian, H.-B. Yao, *ACS Appl. Mater. Interfaces* **2022**, *14*, 17479.
- [6] T. D. Creason, H. Fattal, I. W. Gilley, T. M. McWhorter, M.-H. Du, B. Saporov, *ACS Mater. Au* **2021**, *1*, 62.
- [7] Z. Wang, X. Huang, *Chem. – Eu. J.* **2022**, *28*, e202200609.
- [8] N. Tewari, D. Lam, C. H. A. Li, J. E. Halpert, *APL Mater.* **2022**, *10*, 040905.
- [9] M. T. Vijjapu, S. G. Surya, J.-H. He, K. N. Salama, *ACS Appl. Mater. Interfaces* **2021**, *13*, 40460.
- [10] T. Duong, A. T. John, H. Chen, H. Pham, K. Murugappan, T. Tran-Phu, A. Tricoli, K. Catchpole, *Mater. Adv.* **2022**, *3*, 1263.
- [11] H. Kwak, S. Wang, J. Park, Y. Liu, K. T. Kim, Y. Choi, Y. Mo, Y. S. Jung, *ACS Energy Lett.* **2022**, *7*, 1776.
- [12] Y. Yu, Z. Wang, G. Shao, *J. Mater. Chem. A* **2021**, *9*, 25585.
- [13] J. Liang, X. Li, K. R. Adair, X. Sun, *Acc. Chem. Res.* **2021**, *54*, 1023.
- [14] B.-M. Bresolin, Y. Park, D. W. Bahnemann, *Catalysts* **2020**, *10*, 709.
- [15] A. Nishijima, Y. Kiyozumi, A. Ueno, M. Kurita, H. Hagiwara, T. Sato, N. Todo, *Bull. Chem. Soc. Jpn.* **1979**, *52*, 3724.
- [16] J. Chrištelová, M. Ožvold, *J. Alloys Compd.* **2008**, *457*, 323.
- [17] B. Nalini, S. Selvasekarapandian, K. Janaki, *Phys. Status Solidi B* **1996**, *197*, 13.
- [18] M. Tatsumisago, Y. Shinkuma, T. Minami, *Nature* **1991**, *354*, 217.
- [19] Y. G. Guo, J. S. Lee, J. Maier, *Adv. Mater.* **2005**, *17*, 2815.
- [20] H. Yamada, A. J. Bhattacharyya, J. Maier, *Adv. Funct. Mater.* **2006**, *16*, 525.
- [21] C. Liang, K. Terabe, T. Tsuruoka, M. Osada, T. Hasegawa, M. Aono, *Adv. Funct. Mater.* **2007**, *17*, 1466.
- [22] R. Makiura, T. Yonemura, T. Yamada, M. Yamauchi, R. Ikeda, H. Kitagawa, K. Kato, M. Takata, *Nat. Mater.* **2009**, *8*, 476.
- [23] T. Yamamoto, M. Maesato, N. Hirao, S. I. Kawaguchi, S. Kawaguchi, Y. Ohishi, Y. Kubota, H. Kobayashi, H. Kitagawa, *J. Am. Chem. Soc.* **2017**, *139*, 1392.
- [24] C. Liang, K. Terabe, T. Hasegawa, M. Aono, N. Iyi, *J. Appl. Phys.* **2007**, *102*, 124308.
- [25] A. Hao, C. Gao, M. Li, C. He, X. Huang, G. Zou, Y. Tian, Y. Ma, *J. Appl. Phys.* **2007**, *101*, 053701.
- [26] J. Zheng, B. Perry, Y. Wu, *ACS Mater. Au* **2021**, *1*, 92.
- [27] X. He, Y. Zhu, Y. Mo, *Nat. Commun.* **2017**, *8*, 15893.
- [28] C. Balischewski, K. Behrens, K. Zehbe, C. Günter, S. Mies, E. Sperlich, A. Kelling, A. Taubert, *Chem. – Eur. J.* **2020**, *26*, 17504.
- [29] C. Balischewski, B. Bhattacharyya, E. Sperlich, C. Günter, A. Beqiraj, T. Klamroth, K. Behrens, S. Mies, A. Kelling, S. Lubahn, L. Holtzheimer, A. Nitschke, A. Taubert, *Chem. – Eur. J.* **2022**, *28*, e202201068.
- [30] H.-H. Li, Z.-R. Chen, L.-C. Cheng, M. Feng, H.-D. Zheng, J.-Q. Li, *Dalton Trans.* **2009**, 4888.
- [31] Y. Wang, J. Mo, W. Cai, L. Yao, L. Zhang, *J. Mater. Res.* **2011**, *16*, 990.
- [32] T. Yu, L. An, L. Zhang, J. Shen, Y. Fu, Y. Fu, *Cryst. Growth Design* **2014**, *14*, 3875.
- [33] N. Yang, X. Lv, S. Zhong, D. Qian, S. Han, D. Li, X. Geng, H. Fang, W. Jiang, *Dalton Trans.* **2018**, *47*, 11420.
- [34] H. P. Stephenson, H. Sponer, *J. Am. Chem. Soc.* **1957**, *79*, 2050.
- [35] M. Pagliai, G. Mancini, I. Carnimeo, N. De Mitri, V. Barone, *J. Comput. Chem.* **2017**, *38*, 319.
- [36] A. Abouserie, K. Zehbe, P. Metzner, A. Kelling, C. Günter, U. Schilde, P. Strauch, T. Körzdörfer, A. Taubert, *Eur. J. Inorg. Chem.* **2017**, *2017*, 5640.
- [37] S. C. GmbH, X-Area. software package for collecting single-crystal data on STOE area-detector diffractometers, for image processing, for the correction and scaling of reflection intensities and for outlier rejection, STOE & Cie GmbH, **2018**.
- [38] G. Sheldrick, *Acta Crystallogr. A* **2008**, *64*, 112.
- [39] G. Sheldrick, *Acta Crystallogr. C* **2015**, *71*, 3.
- [40] H. Putz, K. Bandenburg, *Diamond – Crystal and Molecular Structure Visualization, Crystal Impact*, Vol. 102, GbR, Kreuzherrenstr., Bonn, Germany, **2020**, p. 53227, <https://www.crystalimpact.de/diamond>.